

**MODELLING OF GRAPHENE BASED  
MULTIMODE INTERFERENCE WAVEGUIDE AS  
A REFRACTIVE INDEX OPTICAL SENSOR**

**STEPHENIE YEOH**

**UNIVERSITI SAINS MALAYSIA**

**2022**

**MODELLING OF GRAPHENE BASED  
MULTIMODE INTERFERENCE WAVEGUIDE AS  
A REFRACTIVE INDEX OPTICAL SENSOR**

by

**STEPHENIE YEOH**

**Thesis submitted in fulfilment of the requirements  
for the degree of  
Doctor of Philosophy**

**September 2022**

## ACKNOWLEDGEMENT

First and foremost, I would like to thank my main supervisor, Professor Dr. Mohd Zubir Bin Mat Jafri, whose expertise and positive encouragements were invaluable throughout the writing of this dissertation. The completion of my dissertation would not have been possible without my co-supervisor, Dr. Kussay Al-Zubaidi, for the insightful feedback that sharpened my thinking to a higher level. I wish to show my appreciation to my co-supervisor Associate Professor Dr. Lim Hwee San for providing the opportunities and support throughout the research. Special thanks to Dr. Beh Khi Poay for providing scientific guidance and inspiring research ideas. My sincere appreciation to MyBrain scholarship program for the financial support and the following grant schemes, LRGS(2015)/NGOD/UM/KPT, 1001/PFIZIK/811220 and 203/PFIZIK/6711349 for supporting this research. I would like to express my utmost gratitude to my beloved parents for their love, sacrifices and unconditional moral support that allow me to pursue my passion. Many thanks to my colleagues, Dr. Tan Chun Ho, Nursyahida Mohamad Hassan, Dr. Yeap Eong Choon and Dr. Wong Ze-Hao for the exchange of enthusiastic and stimulating discussions. Special thanks to my friends especially Tan Wei Zong and Teh Jay Lin for the emotional support when I hit rock bottom. I am extremely grateful for my pastors, leaders and my dear Alife members for their powerful prayers especially in facing the unprecedented COVID-19 pandemic. Finally, I would like to take this opportunity to praise God for His goodness and providing the faith to trust His strength in overcoming challenges and setbacks. May God bless you and may peace, hope and love be with you always.

STEPHENIE YEOH, 2021

## TABLE OF CONTENTS

<b>ACKNOWLEDGEMENT .....</b>	<b>ii</b>
<b>TABLE OF CONTENTS .....</b>	<b>iii</b>
<b>LIST OF TABLES.....</b>	<b>vi</b>
<b>LIST OF FIGURES.....</b>	<b>vii</b>
<b>LIST OF SYMBOLS .....</b>	<b>xi</b>
<b>LIST OF ABBREVIATIONS .....</b>	<b>xv</b>
<b>LIST OF APPENDICES.....</b>	<b>xvi</b>
<b>ABSTRAK.....</b>	<b>xvii</b>
<b>ABSTRACT .....</b>	<b>xix</b>
<b>CHAPTER 1 INTRODUCTION.....</b>	<b>1</b>
1.1 Background .....	1
1.1.1 Optical Sensor .....	2
1.1.2 Graphene.....	2
1.1.3 Multimode Interference Waveguide.....	4
1.2 Problem Statement .....	5
1.3 Scope of the Study.....	6
1.4 Research Objectives .....	7
1.5 Thesis Outline .....	8
<b>CHAPTER 2 LITERATURE REVIEW .....</b>	<b>9</b>
2.1 Introduction .....	9
2.2 Refractive Index Optical Sensors .....	9
2.2.1 Plasmonic Sensors .....	10
2.2.2 Photonic Sensors .....	11
2.2.3 Research Gap.....	12
2.3 Multimode Interference Waveguide.....	13

2.3.1	Enhancement Layers for Near Field Sensing .....	16
2.3.2	Nanomaterial Integrated Structures .....	16
2.4	Optical Properties of Graphene .....	19
2.4.1	Linear Optical Properties of Graphene .....	20
2.4.2	Nonlinear Optical Properties of Graphene .....	23
2.4.3	All-Optical Modulation with Waveguide .....	25
2.4.4	Fundamental Limits of Graphene .....	28
2.5	Graphene Based Waveguide Sensor .....	29
2.6	Numerical Analysis Methods of Nonlinear Photonic Waveguide .....	31
	<b>CHAPTER 3 NUMERICAL AND SIMULATION METHOD .....</b>	<b>33</b>
3.1	Introduction .....	33
3.2	Maxwell's Equations .....	34
3.3	Modelling Optical Properties of Graphene .....	35
3.4	Distribution in Multilayer Slab Waveguides .....	37
3.4.1	TM Modes Wave Equation .....	39
3.4.2	Dispersion Relation .....	40
3.4.3	Evanescent Wave Equation for Surface Wave Amplification and Sensitivity .....	41
3.4.4	Propagating Power Distribution .....	45
3.5	Finite Difference Time Domain Method (FDTD) .....	47
3.5.1	FDTD Algorithm .....	47
3.5.2	FDTD for Nonlinear Model .....	49
3.6	Simulation of Graphene Based MMI Waveguide .....	50
3.6.1	Characterisation of MMI Waveguide .....	51
3.6.2	Design Requirements and Simulation Boundary Conditions .....	53
3.6.3	Mode Profile Analysis and Power Transmission .....	55

<b>CHAPTER 4 RESULTS AND DISCUSSION .....</b>	<b>59</b>
4.1 Introduction .....	59
4.2 Optical Characterisation of the Graphene Based MMI Waveguide.....	60
4.2.1 Linear Optical Properties of Graphene.....	61
4.2.2 Nonlinear Optical Properties of Graphene .....	64
4.2.3 Structural Optimisation of MMI Waveguide .....	65
4.3 Numerical Analysis of Electromagnetic Field Propagating in Graphene Based Waveguide Structure .....	67
4.3.1 Modal Field Analysis and Dispersion Characteristic .....	68
4.3.2 Modal Fields Analysis.....	71
4.4 Refractive Index Sensing Performance .....	75
4.4.1 Evanescent Field Sensing.....	76
4.4.2 Effect of Thickness on the Surface Sensitivity.....	83
4.4.3 Output Power Distribution .....	89
4.5 OptiFDTD Simulation.....	92
4.5.1 Field Distribution and Refractive Index Analysis .....	93
4.5.2 Output Power Analysis.....	98
4.5.3 Cladding Power Analysis .....	100
4.5.4 Spectral Analysis .....	101
4.6 High Power Analysis.....	105
4.7 Performance Comparison.....	111
<b>CHAPTER 5 CONCLUSION AND RECOMMENDATIONS.....</b>	<b>114</b>
5.1 Conclusion.....	114
5.2 Recommendation and Future Works.....	116
<b>REFERENCES .....</b>	<b>117</b>
<b>APPENDICES</b>	
<b>LIST OF PUBLICATIONS</b>	

## LIST OF TABLES

		<b>Page</b>
Table 2.1	Basic properties of most researched 2D materials for optical devices .....	19
Table 2.2	The reported values of refractive index, $n_{gr}$ and the calculated $\sigma_{gr}$ for monolayer, multilayer graphene and graphite in literature .....	21
Table 3.1	Structure's parameter of weakly guiding MMI waveguide .....	53
Table 4.1	The parameters of the linear and nonlinear graphene based MMI sensor.....	110
Table 4.2	Performance and sensitivity of MMI sensors in literature .....	112

## LIST OF FIGURES

		Page
Figure 1.1	Graphene hexagonal lattice structure with each carbon atom is covalently bonded to three other carbon atoms interacting with -OH bonds from the aqueous surrounding.....	3
Figure 2.1	Schematic diagram of a dielectric slab waveguide .....	15
Figure 2.1	Structures of a) zero-dimensional (0D) nanoparticles, b) one-dimensional (1D) nanotubes, c) 2D nanosheets and d) 3D nanostructures .....	17
Figure 3.1	Process of deriving dispersion relation to obtain the homogeneous surface sensitivity and power distribution of each layer .....	34
Figure 3.2	The schematic layout of a basic planar dielectric optical waveguide structure .....	38
Figure 3.3	The FDTD explicit algorithm .....	48
Figure 3.4	Process of building a layout for waveguide in layout designer ..	51
Figure 3.5	The $xz$ -cross-sectional plane of multilayer planar waveguide structure as captured in OptiFDTD Layout Designer in micrometre dimension .....	52
Figure 3.6	The boundary conditions parameters .....	55
Figure 3.7	The wavelength 1.55 $\mu\text{m}$ Gaussian modulated continuous wave defined in input field properties in OptiFDTD .....	56
Figure 4.1	Process of numerical evaluation for a multilayer waveguide .....	56
Figure 4.2	Linear complex optical conductivity of monolayer graphene, $\sigma_{gr}$ against frequency, $f$ .....	62
Figure 4.3	Linear complex permittivity of graphene, $\epsilon_{gr}$ against wavelength, $\lambda$ .....	62
Figure 4.4	Linear complex RI of graphene, $n_{gr}$ against wavelength, $\lambda$ .....	63

Figure 4.5	Third order conductivity, $\sigma_{gr}^{(3)}$ of monolayer graphene against wavelength, $\lambda$ .....	64
Figure 4.6	RI profile of the proposed graphene on MMI waveguide (as denoted in prior, $n_{gr} = n_1$ and $n_{surr} = n_4$ ) .....	66
Figure 4.7	The effective refractive index, $N_{eff}$ variations with propagation constant, $\beta$ .....	68
Figure 4.8	Graphical plots of the dispersion function, $F$ to calculate the characteristic behaviour of propagation constant of TM modes	69
Figure 4.9	The effective refractive index, $N_{eff}$ as a function of core thickness, $h$ for the graphene based MMI waveguide .....	71
Figure 4.10	Calculated a) magnetic field, $H_y$ and b) electric field, $E_x$ distributions of TM modes ( $m = 0, 1, 2$ ) in graphene on waveguide with 6 $\mu\text{m}$ thick core.....	73
Figure 4.11	Calculated a) magnetic field, $H_y$ b) electric field, $E_x$ distributions of $\text{TM}_0$ in the waveguide with core thickness, $h$ at 2 $\mu\text{m}$ , 4 $\mu\text{m}$ and 6 $\mu\text{m}$ .....	74
Figure 4.12	The dependence of the effective refractive index, $N_{eff}$ on RI of the surrounding medium, $n_{surr}$ of TM modes ( $m = 0, 1, 2$ ).....	76
Figure 4.13	Calculated a) magnetic field, $H_y$ and b) electric field, $E_x$ distributions of $\text{TM}_0$ modes at the sensing environment of 6 $\mu\text{m}$ thick core waveguide for a range of $n_{surr}$ .....	78
Figure 4.14	Calculated a) magnetic field, $H_y$ and b) electric field, $E_x$ distributions of $\text{TM}_1$ modes at the sensing environment of 6 $\mu\text{m}$ thick core waveguide for a range of $n_{surr}$ .....	79
Figure 4.15	Calculated a) magnetic field, $H_y$ and b) electric field, $E_x$ distributions of $\text{TM}_2$ modes at the sensing environment of 6 $\mu\text{m}$ thick core waveguide for a range of $n_{surr}$ .....	80
Figure 4.16	The penetration depth, $d_p$ as a function of core layer thickness, $h$ .....	82
Figure 4.17	The penetration depth, $d_p$ in the cladding layer against $n_{surr}$ of TM modes ( $m = 0, 1, 2$ ).....	83
Figure 4.18	The calculated sensitivity, $Re[s_h]$ against $h$ for three-layer and four-layer MMI waveguide.....	85

Figure 4.19	Surface sensitivity, $Re[S_h]$ against effective index, $N_{eff}$ for different $d_{gr}$ .....	86
Figure 4.20	Surface sensitivity, $Re[S_h]$ against $n_{surr}$ at different value of $d_{gr}$ .....	87
Figure 4.21	The estimated number of layers, $N_{SLG}$ of monolayer graphene with $d_{gr}$ .....	88
Figure 4.22	The power flowing in the core layer, $P_2$ per total power against $n_{surr}$ .....	90
Figure 4.23	The power flowing in the surrounding medium, $P_{surr}$ per total power against $n_{surr}$ .....	90
Figure 4.24	The power flowing in the substrate layer, $P_3$ per total power against $n_{surr}$ .....	91
Figure 4.25	The power flowing in the graphene layer, $P_{gr}$ per total power against $n_{surr}$ .....	91
Figure 4.26	RI distribution of the proposed sensor in the $xz$ -plane exported from OptiFDTD .....	93
Figure 4.27	The top view of $H_y$ propagating in the $z$ -direction simulated using OptiFDTD .....	94
Figure 4.28	Amplitude, $H_y$ against the propagation distance, $z$ .....	95
Figure 4.29	Field distribution of $H_y$ of reference sensor at the input power $1.00E-8$ W/ $\mu$ m .....	97
Figure 4.30	Field distribution of $H_y$ of graphene sensor at the input power $1.00E-8$ W/ $\mu$ m .....	97
Figure 4.31	Field distribution of $H_y$ of nonlinear sensor at the input power $5.00E6$ W/ $\mu$ m .....	98
Figure 4.32	The normalised propagating output power, $P_{out}$ against $n_{surr}$ of reference and graphene sensors .....	99
Figure 4.33	Sensitivity, $S_p$ against $n_{surr}$ of reference and graphene sensors .....	100
Figure 4.34	The normalised surface power at the cladding, $P_{gr}$ against $n_{surr}$ .....	101
Figure 4.35	Normalised propagating power of (a) graphene sensor and (b) reference sensor against wavelength, $\lambda$ .....	102

Figure 4.36	Relative propagating power of graphene based MMI waveguide against wavelength, $\lambda$ at the input power $1.00E-8$ W/ $\mu$ m .....	104
Figure 4.37	Peak wavelength, $\lambda_{peak}$ against $n_{surr}$ of graphene sensor.....	105
Figure 4.38	FWHM of the graphene sensor as a function of $n_{surr}$ .....	105
Figure 4.39	Relative propagating power of graphene based MMI waveguide against wavelength, $\lambda$ at different input power in the order $1.00E6$ W/ $\mu$ m .....	107
Figure 4.40	Relative propagating power of graphene sensor against wavelength, $\lambda$ at the input power $5.00E6$ W/ $\mu$ m .....	108
Figure 4.41	Peak wavelength, $\lambda_{peak}$ against $n_{surr}$ of nonlinear sensor at the input power $5.00E6$ W/ $\mu$ m.....	109
Figure 4.42	FWHM of the nonlinear sensor as a function of $n_{surr}$ .....	109

## LIST OF SYMBOLS

$\bar{S}_h$	Surface sensitivity of three-layer waveguide
A, B, C, D, G <sub>1</sub> , G <sub>2</sub>	Field constants
Ag	Silver
Au	Gold
B	Magnetic flux density
BaTiO <sub>3</sub>	Barium Titanate
$c_m$	Field excitation coefficients
D	Electric flux density
$d_{gr}$	Thickness of the graphene layer
$d_p$	Penetration depth
e	Electron mass
E	Electric field
$E(\omega)$	Electric field strength
$E_f$	Fermi level
$E_x$	Electric field along the $x$ -axis
F	Function of dispersion equation
$h$	Thickness of core
H	Magnetic field
$\hbar$	Planck constant
$H_y$	Magnetic field along the $y$ -axis
$Im[\sigma_{gr}]$	Imaginary part of the optical conductivity of graphene
$\kappa_B$	Boltzmann constant
$L_{MMI}$	Length of MMI

$L_{\pi}$	Beat length of the two lowest modes
$n_0$	Linear refractive index
$n_1$	Refractive index of cladding
$n_2$	Refractive index of core
$n_3$	Refractive index of substrate
$n_4$	Refractive index of surrounding medium
$N_{eff}$	Effective refractive index
$n_{gr}$	Refractive index of graphene
$N_{SLG}$	Number of monolayer graphene
OLH	Horizontal observation line
OLV	Vertical observation line
$P_2$	Propagating power in core
$P_3$	Propagating power in substrate
$P_{gr}$	Propagating power in graphene
$P_{measured}$	Propagating power of graphene sensor
$P_{norm}$	Normalised propagating power
$P_{out}$	Output power
$P_{reference}$	Propagating power of reference sensor
$P_{rel}$	Relative propagating power
$P_{surr}$	Propagating power in surrounding medium
$P_{total}$	Total guided wave power
$Q_{1,2}, \bar{Q}_{1,2}$	Variables of dispersion equation
$R^2$	The coefficient of determination
$Re[n_{gr}]$	Real part of the refractive index of graphene
$Re[S_h]$	Real part of surface sensitivity

$Re[\varepsilon_{gr}]$	Real part of the permittivity of graphene
$Re[\sigma_{gr}]$	Real part of the optical conductivity of graphene
$S_h$	Surface sensitivity
$S_p$	Sensitivity of the output power
$S_{RI}$	RI sensitivity
$T$	Temperature
$t$	Time
$T_1, T_2$	Variables of dispersion function
$TiO_2$	Titanium dioxide
$U_1, U_2$	Variables of $Q_1$
$W_e$	Effective width
$W_{MMI}$	Width of MMI
$WO_3$	Tungsten trioxide
$\beta$	Propagation constant
$\beta_m$	Propagation constant of $m$ mode number
$\gamma_1$	Propagation constant of cladding
$\gamma_{layer}$	Layer propagation constant
$\gamma_2$	Propagation constant of core
$\gamma_3$	Propagation constant of substrate
$\gamma_4$	Propagation constant of surrounding medium
$\Delta$	Atomic thickness of monolayer graphene
$\varepsilon$	Dielectric permittivity
$\varepsilon_0$	Dielectric permittivity in vacuum
$\varepsilon_1$	Permittivity of cladding
$\varepsilon_{layer}$	Layer permittivity

$\varepsilon_2$	Permittivity of core
$\varepsilon_3$	Permittivity of substrate
$\varepsilon_4$	Permittivity of surrounding medium
$\varepsilon_{gr}$	Relative complex permittivity of graphene
$\varepsilon_r$	Relative dielectric permittivity
$\lambda$	Wavelength
$\lambda_0$	Free space wavelength
$\lambda_{peak}$	Peak wavelength
$\lambda_{shift}$	Wavelength shift
$\mu$	Magnetic permeability
$\mu_0$	Magnetic permeability in vacuum
$\xi_{1,2,3,4,5,6,7,8,9,10,11,12,13}$	Variables of dispersion function
$\rho$	Flux density
$\sigma_0$	Universal dynamic conductivity
$\sigma_{gr}$	Complex linear optical conductivity of graphene
$\sigma_{gr}^{(3)}$	Third-order optical conductivity
$\nu_1$	First relaxation frequency
$\nu_2$	Second relaxation frequency
$\chi^{(1)}$	Linear susceptibility
$\chi^{(3)}$	Third-order susceptibility
$\chi_{1,2,3}$	Variables of dispersion function
$\chi_{eff}$	Effective susceptibility
$\chi_{gr}^{(3)}$	Third-order susceptibility of graphene
$\Psi$	Propagation constant of m mode number
$\omega$	Angular frequency

## LIST OF ABBREVIATIONS

0D	Zero-Dimensional
1D	One-Dimensional
2D	Two-Dimensional
3D	Three-Dimensional
APML	Anisotropic Perfectly Matched Layer
BPM	Beam Propagation Method
EM	Electromagnetic
FDTD	Finite-Difference Time-Domain
FEM	Finite Element Method
FOM	Figure Of Merit
FPI	Fabry Perot Interferometer
FWHM	Full Width at Half Maximum
FWM	Four-Wave Mixing
IR	Infrared
MMI	Multimode Interference
MZI	Mach-Zehnder Interferometer
NIR	Near-Infrared
PBC	Periodic Boundary Condition
RAM	Random-Access Memory
RI	Refractive Index
RIU	Refractive Index Unit
SMF	Single Mode Fibre
SPP	Surface Plasmon Polariton
SPR	Surface Plasmon Resonance
TE	Transverse Electric
THG	Third-Harmonic Generation
THz	Terahertz
TIR	Total Internal Reflection
TM	Transverse Magnetic
USM	University Sains Malaysia
UV	Ultraviolet

## LIST OF APPENDICES

- Appendix A Derivation of dispersion relation of the slab waveguide structure for TM mode
- Appendix B Propagation constants for change in thickness of core layer for three-layer and four-layer MMI waveguide ( $n_{surr} = 1.333$ )

**PEMODELAN PANDU GELOMBANG INTERFERENS MULTIMOD  
BERASASKAN GRAFENE SEBAGAI PENGESAN OPTIK INDEKS BIASAN**

**ABSTRAK**

Sejak beberapa tahun kebelakangan ini, permintaan untuk alat pengesan yang padat, mudah alih, sensitif dan mudah difabrikasi berkembang dengan pesat untuk aplikasi industri, perubatan dan persekitaran. Namun, ia tetap menjadi cabaran untuk meminimumkan peranti serta memastikan kepekaan yang tinggi dan pengesan yang efisien dalam julat panjang gelombang yang luas. Peranti yang canggih mengalami kehilangan yang tinggi dan julat pengesanan analit yang kecil di kawasan spektrum inframerah dekat (NIR). Penyelidikan ini mengatasi masalah ini dengan menyepadukan grafene pada struktur interferens multimod (MMI) yang terdiri daripada pandu gelombang dielektrik satah yang dibatasi oleh substrat dan lapisan pelapis. Indeks biasan (RI) lapisan grafene yang tinggi menyebabkan mod kurang terkurung di bahagian teras. Peningkatan medan lenyap pada permukaan pandu gelombang menghasilkan kepekaan yang lebih tinggi terhadap perubahan RI dalam medium di sekitarnya. Hubungan penyebaran mod magnet melintang (TM) diperoleh daripada persamaan Maxwell untuk menyiasat kesan parameter geometri dan optik termasuk ketebalan, kekonduksian dan indeks biasan. Grafene dimodelkan sebagai filem homogen dengan ketebalan terhingga untuk menyiasat kepekaan indeks biasan berkesan ( $N_{eff}$ ) terhadap variasi RI medium di sekitarnya. Dalam penyelidikan ini, kaedah komputasi yang digunakan untuk mensimulasikan grafene adalah kaedah domain masa perbezaan terhingga (FDTD). Dengan menggunakan pakej perisian komersial OptiFDTD, grafene dimodelkan sebagai permukaan tipis yang menempati sebahagian kecil sel FDTD. Keamatan cahaya yang dipancarkan dan spektrum

pancaran pada pengeluaran diukur sebagai tindak balas perubahan RI dalam medium di sekitarnya. Penggabungan grafene dapat mengurangkan turun naik kuasa pengeluaran dengan ketara yang disebabkan oleh isyarat pengeluaran berkala pandu gelombang MMI. Peningkatan RI oleh medium di sekitar menganjak kedudukan spektrum ke arah panjang gelombang yang lebih panjang. Pengesan RI berasaskan grafene yang dimodelkan mencapai kepekaan  $2.666 \mu\text{m}/\text{RIU}$ , lebar penuh pada separuh maksimum (FWHM) ialah  $0.068$  dan nilai merit (FOM) ialah  $39 \text{RIU}^{-1}$  dalam julat pengukuran RI daripada  $1.333$  hingga  $1.400$ . Pengaruh kesan tak linear grafene pada pandu gelombang MMI disiasat dengan memodulasi kuasa input dalam turutan  $1.00\text{E}6 \text{ W}/\mu\text{m}$ . Pengesan RI tak linear mencapai kepekaan sebanyak  $2.570 \mu\text{m}/\text{RIU}$ , FWHM ialah  $0.496$  dan FOM ialah  $5 \text{RIU}^{-1}$ . Pengesan tak linear panjang gelombang terpilih berpotensi besar dalam modulasi dinamik panjang gelombang puncak untuk membezakan sampel yang diuji dengan mengubah keamatan input. Pengesan tak membinasa dan tak invasif semua optik yang dicadangkan mempunyai potensi yang tinggi untuk aplikasi jarak dekat dan masa nyata dalam penyelidikan bioperubatan, diagnos tempat penjagaan, pemantauan alam sekitar dan kawalan bekalan air.

# MODELLING OF GRAPHENE BASED MULTIMODE INTERFERENCE WAVEGUIDE AS A REFRACTIVE INDEX OPTICAL SENSOR

## ABSTRACT

Over the recent years, demands for compact, portable, sensitive and easy to fabricate sensing devices have grown rapidly for industrial, medical and environmental applications. However, it remains a challenge to miniaturise the device while ensuring high sensitivity and efficient sensing in a wide range of wavelength. The state-of-the-art devices suffer from high losses and narrow detection range of analytes at the near-infrared (NIR) spectral regions. This research overcomes these issues by integrating graphene on a multimode interference (MMI) structure which is composed of a dielectric planar waveguide confined by a substrate and a cladding layer. The high refractive index (RI) of graphene layer of 2.345 causes the modes to be less confined in the core region. The enhancement of evanescent field on the surface of the waveguide results in higher sensitivity to changing RI in surrounding medium. The dispersion relation of transverse magnetic (TM) modes is derived from Maxwell's equations to investigate the impact of the geometric and optical parameters including thickness, conductivity and refractive indices. Graphene is modelled as a homogeneous film with finite thickness to investigate the sensitivity of the effective refractive index ( $N_{eff}$ ) to variations in the RI of the surrounding medium. In this research, the computational method used to simulate graphene is finite-difference time-domain (FDTD) method. Using the commercial software package OptiFDTD, graphene is modelled as a thin surface occupying a fraction of FDTD cell. The transmitted light intensity and the transmission spectra at the output were measured as a response of change in RI in the surrounding medium. The incorporation of graphene

is found to have lesser output power fluctuations that is caused by periodic output signal of the MMI waveguide than the MMI waveguide without graphene. The increase in RI of surrounding medium shifted the spectral position towards the longer wavelength from 0.94  $\mu\text{m}$  to 1.12  $\mu\text{m}$ . The modelled graphene based RI sensor achieved sensitivity of 2.666  $\mu\text{m}/\text{RIU}$ , full width at half maximum (FWHM) of 0.068 and figure of merit (FOM) of 39  $\text{RIU}^{-1}$  in the measurement range of RI from 1.333 to 1.400. The influence of the nonlinear effects of graphene on the MMI waveguide is investigated by modulating the input power in the order of  $1.00\text{E}6 \text{ W}/\mu\text{m}$ . The nonlinear RI sensor achieved sensitivity of 2.570  $\mu\text{m}/\text{RIU}$ , FWHM of 0.496 and FOM of 5  $\text{RIU}^{-1}$ . The wavelength-selective nonlinear sensor has great potential in the dynamic modulation of the peak wavelengths to discriminate the tested samples via optical modulation. The all-optic non-invasive and non-destructive RI sensor proposed has high potential for near-field and real-time applications in biomedical researches, point-of-care diagnosis, environmental monitoring and water supply control.

## CHAPTER 1

### INTRODUCTION

#### 1.1 Background

Intense research efforts are being directed towards developing compact, cost-effective, efficient, rapid response, broadband and high-performance optical refractive index (RI) sensors for industrial, medical and environmental applications. Optical sensors are capable to translate the change in various parameters such as RI, concentration of liquid or gas, turbidity, temperature or current into optical signals in the forms of observable changes in wavelength, intensity or phase shift (Hu et al., 2017; Lim et al., 2011; Rastgordani & Kashani, 2020; Yeoh et al., 2019). The recent advancement of nanotechnology has revolutionised optical sensors in terms of improved limits of detection and high responsivity (Shivnanju et al., 2019). Two-dimensional (2D) materials are naturally established as promising candidates for sensing devices due to their atomically thin layered structures and high surface-to-volume ratio. Since the isolation of graphene by Andre Geim and Konstantin Novoselov, it has been vastly integrated into novel electro-optical devices due to its exceptional and remarkable electronic, photonic and mechanical properties (Novoselov et al., 2004). Graphene integrated on interferometric optical waveguide is highly sensitive and capable of single-molecule detection (Arjmandi-Tash et al., 2016; Schedin et al., 2007). Interferometric waveguide has the advantages of flexibility in integrating with any preferred materials as well as ability to interconnect with various devices of a photonic integrated circuit. Therefore, this work aims to integrate graphene on an interferometric optical waveguide as a compact and high-performance RI sensor.

### **1.1.1 Optical Sensor**

In the last decade, optical sensors were under extensive development in the field of real-time environmental monitoring, biological sensing and human health diagnosis. Optical sensors have the advantages of being sensitive, immune to electromagnetic (EM) interference, robust and high durability under extreme temperature and pressure. Nanoparticles-based sensors have been extensively utilised for analysing toxins, metal ions and inorganic and organic pollutants (Cheon & Lee, 2008; Wang & Ma, 2009). Optical sensors have robust application in medical application including monitoring blood glucose level, proteins concentration level, pH, urea and inflammatory markers (Jo et al., 2017; Li et al., 2016; Menon et al., 2018; Rauf et al., 2016; Yi et al., 2019). Researchers are actively developing optical sensors to improve the spatial resolution and monitored length range and reduce the susceptibility to physical damage and interference from environmental effects. The atomically thin layered structures of 2D materials are excellent as novel optical sensing devices for broadband detection. The capability of graphene to enhance light-matter interaction were exploited as highly sensitive RI sensors (C. Li et al., 2019; Rastgordani & Kashani, 2020; Sun et al., 2019).

### **1.1.2 Graphene**

The name graphene was introduced by Boehm, Setton and Stumpp (1985). Geim and Novoselov (2005) isolated a single sheet graphene with a simple technique called the “adhesive tape method”. Graphene is a 2D one-atom-thick nanomaterial comprised of  $sp^2$  carbon atoms arranged in a honeycomb crystal lattice structure. Figure 1.1 shows the honeycomb structure consists of a hexagonal Bravais lattice with two basis atoms interacting with -OH bonds from the aqueous surrounding. The carbon-carbon bond length

is 1.42 Å with interplanar spacing of 3.45 Å. Graphene has attracted great research interest among scientists due to its unique properties, including high specific surface area of 2600 m<sup>2</sup>g<sup>-1</sup>, excellent thermal conductivities of 5000 Wm<sup>-1</sup>K<sup>-1</sup>, high levels of stiffness and strength with Young's modulus of approximately 1000 GPa and breaking strength of 130 GPa. The high-speed electron mobility of 200000 cm<sup>2</sup>V<sup>-1</sup>s<sup>-1</sup> at room temperature coupled with 2.3% absorption in the visible and near-infrared (NIR) region grant to ultrafast and efficient all-optical devices (Ono et al., 2020; Saito & Souza, 2019). The high surface to volume ratio of graphene combined with its unique electrical properties offer high sensitivities due to the large number of available molecular binding sites. The capability of graphene interacting with a single molecule, the smallest quantum of resultant change in conduction of measured analytes, is desirable for ultrasensitive sensor application (Geim & Novoselov, 2007).

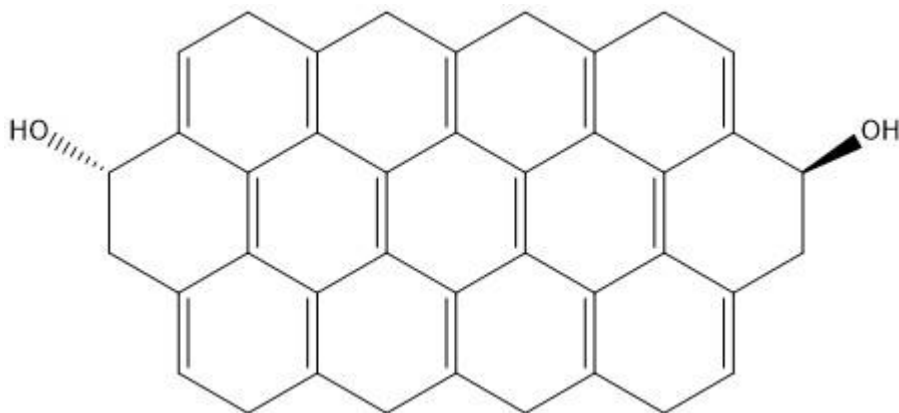


Figure 1.1 Graphene hexagonal lattice structure with each carbon atom is covalently bonded to three other carbon atoms interacting with -OH bonds from the aqueous surrounding.

One of the approaches to increase the responsivity of graphene is by integrating it on the surface of an optical waveguide. The induced evanescent field on the surface of waveguide offers higher light-matter interaction. At the boundary between the waveguide and graphene layer, the modal intensity that is trapped at resonant frequency produced significant interaction length. The ability of graphene to respond to the changes in optical parameters in the external measured medium qualifies it as a valuable candidate to be integrated as optical sensors. Furthermore, the ability to designate the desired number of input and output arbitrarily with the flexibility in fabricating each layer with any preferred material and easy integration into photonics circuits are some of the advantageous of employing multimode interference (MMI) structures.

### **1.1.3 Multimode Interference Waveguide**

A basic three-layer MMI structure consists of a high index medium as a means to confine light propagation, that is sandwiched by dielectric layers (Medri & Gauthier, 2011). The MMI devices have been heavily explored over the years to be exploited in optical devices including modulators, switches and couplers (Barkman et al., 2013; Lien et al., 2002; Thomson et al., 2010). They are attractive in terms of the compact size, easy fabrication and genuine fabrication tolerant power splitting ratios, robustness and low loss. The phenomenon of which an input field profile is reproduced in single or multiple images at periodic intervals along the propagation direction of the multimode waveguide is universally known as self-imaging effect. Self-imaging effect for objects illuminated by coherent light was first discussed by Talbot (1836) and optical MMI devices based on self-imaging effect was illustrated in 1995 (Soldano & Pennings, 1995).

The first MMI waveguide attempted for sensor applications were based on silicon dioxide-titanium dioxide ( $\text{SiO}_2\text{-TiO}_2$ ) (Lukosz, 1991; Schmitt & Hoffmann, 2009). MMI structures that comprise of optical fibres have been numerically and experimentally demonstrated as RI and temperature sensors to unleash the potential of MMI as a compact, ultra-sensitive and large bandwidth device (Fuentes-Fuentes et al., 2015; Li et al., 2014).

Self-imaging phenomena in periodic dielectric waveguides were reported by Zeng et. Al (2009). The self-imaging pattern are modulated by the change in the RI of the core and cladding of the MMI waveguide. The modulation of self-imaging pattern by changing the effective RI of the MMI waveguide comes at the cost of complicated process using high precision mechanical devices. Shi et al. (2015) demonstrated the real-time tuning of self-imaging effects using a hybrid optofluidic waveguide while having the flexibility of controlling the flow rates and liquid materials. The basic theory and analytical solution for the three-layer structure have been widely described and extended to address multilayer structures with dielectric overlays (Medri & Gauthier, 2011) which will be discussed extensively in Chapter 2.

## **1.2 Problem Statement**

The performance of electro-optic devices is largely restricted by the footprint, signal processing speed and figure of merit (FOM) of electronic instruments. All-optical devices are competitive as ultrasensitive, high resolution and high bandwidth solutions. Compact, high-speed and ultrasensitive all-optical devices operating at NIR region while offering simple setup have high research interest for various applications. However, the major hurdles of plasmonic sensors are the tedious alignment requirements that induces coupling

loss and the EM excitations at metal and dielectric surface also suffer significant optical losses in the NIR region (Khurgin & Boltasseva, 2012; O'Hara et al., 2005). Research in all-optical RI sensor to overcome the issue of high optical loss in the NIR region is important.

High quality graphene is costly to synthesise in large production. Therefore, developing reproducible graphene-based optical sensors with minimal susceptibility to the quality and thickness of mass-produced graphene is desirable. The proposed graphene based MMI sensor modelled with finite-difference time-domain (FDTD) method shall pave way for miniaturised, ultrasensitive, dynamic tunability and high bandwidth all-optical sensors.

### **1.3 Scope of the Study**

In this research, a 2D simulation model is designed and analysed using the software OptiFDTD to describe the EM field propagating in a graphene based MMI waveguide. The operating light source with central peak wavelength  $1.55 \mu\text{m}$  that is in the telecommunication wavelength is compatible with the fibre optics infrastructure and silicon photonics; thus, lowering the cost of integrated optical components. For simplicity, the optical properties of the materials are lossless, isotropic and homogeneous. The optical properties of the materials are characterised by defining the real part of their optical while the imaginary part that is accountable for the material's linear absorption is assumed negligible for simplification. The RI measurement range used to investigate sensing performance in this study is from 1.333 to 1.400, as proposed in most literatures for

aqueous solutions and biosensing application (Guzmán-Sepúlveda et al., 2013; Li, 2020; Wang et al., 2017). In the FDTD method, the minimum mesh size and proper number of steps used in the simulation software is  $0.05 \mu\text{m}$  and 5200 respectively for optimum computation time and memory without compensating the accuracy. The dispersion relation of graphene based MMI is investigated to improve its sensitivity towards the RI change in the surrounding medium. The surface sensitivity analysis and calculations of optimum parameters were performed using the MATLAB software. The proposed RI sensor has potential in sensitive real-time monitoring in environmental and medical applications.

#### **1.4 Research Objectives**

The proposed work aims to design and analyse a graphene based MMI waveguide as an optical RI sensor that offers simple setup with enhanced light-matter interaction in the NIR region using OptiFDTD software. The objectives of this study are as follows:

1. To investigate the dispersion characteristics of propagating transverse magnetic (TM) modes in a graphene based MMI waveguide by building a four-layer dispersion model
2. To design and simulate the propagation of TM modes in a four-layer graphene-based MMI waveguide via FDTD method based on the optimum parameters obtained from the dispersion model
3. To model graphene on MMI as an RI optical sensor in liquid of index of refraction from 1.333 to 1.400 in the NIR region

4. To simulate and investigate the performance of nonlinearity of graphene on the MMI waveguide using high power light source

## **1.5 Thesis Outline**

This thesis consists of five chapters. Literature reviews will be covered in Chapter 2 which include the fundamental properties of graphene and the current works by researchers in MMI waveguide applied as optical sensors. Chapter 3 describes the numerical and simulation method to characterise EM field propagating in graphene based MMI waveguide. Chapter 4 presents the simulation outcomes with a discussion of the analysed results. Chapter 5 summarises all the output and result of this research with recommendation for future study. Finally, the derivation of dispersion equation and the calculated propagation constant of MMI waveguide will be included in the appendices.

## CHAPTER 2

### LITERATURE REVIEW

#### 2.1 Introduction

An overview to the previous works of the general types of optical RI sensors with plasmonic and photonic structures are reviewed. The advanced and trending enhancement layers integrated on multimode waveguides for near field sensing are also discussed. Next, the fundamentals and principles of linear and nonlinear optical properties of graphene and its nonlinear effects are briefly summarised. Graphene integrated on waveguides for all-optical modulation and its fundamental limits are also described in the next section. Subsequently, the state-of-the-art realistic photonics applications of graphene sensors are reviewed to fully demonstrate its potential to revolutionise highly efficient all-optical sensors. The existing approaches used in numerical analysis and commercial software available that simulates the field propagation in photonic waveguides are reviewed. Finally, the main findings of the recent developments of RI sensors in literature is summarised.

#### 2.2 Refractive Index Optical Sensors

The optical RI sensors are highly suitable for industrial, environmental monitoring and medical diagnostic applications for being the remarkable solutions to high-speed, compact and sensitive sensor. At the current rate of development of optical sensors are progressing, the optical RI sensors have higher potential in enabling new technologies to emerge than the matured development of electronic sensors (Danaie & Kiani, 2018; Joe et al., 2018; Qian et al., 2018; K. Xu et al., 2019; Y. Xu et al., 2019). The RI measurements can be

interpreted in terms of changes in liquid concentration, gas concentration, turbidity, pH and humidity (Chyad et al., 2013; Dick et al., 2007; Duarte et al., 2020; Gu et al., 2009; Leal-Junior et al., 2018). Modern RI sensors that perform sensing measurements in an aqueous environment would typically cover a wide range of index of refractive from 1.333 to 1.400 (Jorgenson & Yee, 1994; Sequeira et al., 2016).

Generally, optical RI sensors can be divided into two types, plasmonic sensors and photonic sensors. Plasmonic sensors are commonly built on metallic structures to excite the propagating or localised surface plasmon on the metal surface. Plasmonic sensors are generally more sensitive to the change of the environment and operates in a wide working wavelength from visible to NIR. However, metal-based plasmonic RI sensors are usually lossy with broad spectral line-width of resonance curves resulting in poorer precision and accuracy. Furthermore, metals are prone to oxidation and corrosion under high temperatures which limit their applications in harsh environments. On the other hand, photonic RI sensors are built on dielectric structures to excite the surface EM wave propagating at the dielectric interface. The dielectric-based photonic RI sensors are nearly lossless and tend to have sharper resonance curves. Hence, they offer better precision and accuracy and operate at NIR wavelength range. As a trade-off, they have lower mode confinement than the plasmonic sensors.

### **2.2.1 Plasmonic Sensors**

Liedberg et al. (1983) were the first to experimentally demonstrate plasmonic sensor using prism coupling technique. Surface plasmon resonance (SPR) effect is created when a TM polarised light is incident at the metal layer on a prism and eventually excites the surface

plasmon polariton (SPP) on the metal-prism surface. In addition to being sensitive to the change in environment, SPP is distinguishable through shift in resonance angle, resonance wavelength, phase or intensity variations. Prism coupling sensors are bulky and the tedious configuration and alignment makes it inconvenient for long range sensing. SPR sensors developed by coating metals such as silver (Ag) and gold (Au) on polished optical waveguides has improved in sensitivity with dynamic sensing range (Mollah et al., 2019; Zainuddin et al., 2019). However, in addition to the requirement of precise polishing technique, the oxidation of metal hinders the precise control of plasmonic resonance.

### **2.2.2 Photonic Sensors**

The common photonic sensors are dielectric-based waveguide structure. The fabrication of dielectric slab waveguide as an integrated optical sensor was first presented by Teifenthelar and Lukosz (1984). The principle involves EM field being totally internally guided in the core waveguide and at every point of reflection at the boundary, evanescent field is formed at the interface and decays into the surrounding medium. The intensity at the output changes when the evanescent field interacts with analytes. The perturbations in the evanescent field can be monitored through changes in  $N_{eff}$  of the guided modes, absorption, phase, polarisation, frequency or luminescence. Generally, dielectric-based RI sensors have low loss hence sharper resonances due to the low extinction coefficients of dielectrics. They are also intrinsically inert to the ambient chemicals. Next development in optical sensors may also take advantage from the advances in integrating functional materials onto optical waveguides. The most widely used configuration in photonic RI sensors is the interferometer configuration.

### 2.2.3 Research Gap

Plasmonic sensors have been widely implemented for the extraordinary sensitivity and effective light confinement. However, the bulky conventional plasmonic RI sensors require tedious configuration and alignment that are inconvenient for real-time and remote sensing (O'Hara et al., 2005). While the sensitivity of metal enhanced RI sensors leads to improvement, they are costly, prone to oxidation and corrosion under high temperatures which limit their applications in harsh environments (Mollah et al., 2019; Zainuddin et al., 2019). Moreover, the attenuation and surface reflection of metals are likely to compromise their sensitivities (Gan et al., 2012; Shiue et al., 2013; Zhao et al., 2014). Other plasmonic waveguides with complex and delicate configurations using nano- or micro-structure as well as metal gratings suffer from narrow bandwidth. In contrast, the highly sensitive and mechanically strong nanomaterials such as graphene are often used as oxidation resist layer. Furthermore, the high mobility of the carrier and adsorption capabilities to ions and molecules thereby improve the sensitivity.

Numerous research on structurally modified plasmonic sensors such as polished or tapered fibres have been proposed. Recent advances in optoelectronics have motivated the development of novel optical fibre sensors to measure RI. Optical fibre sensors have the advantages of EM immunity, low cost, small footprint and their remote sensing capability. Modification have also been exploited for RI sensing with unclad fibres with metal layers deposited on the core, side-polished fibres or tapered fibres (Gangwar et al., 2021; Zhao et al., 2016). Optical fibres with modified fibre-end-face, such as metallic mirror and metal-coated angled fibre tip have also been employed to improve sensitivity (R. Humud et al., 2018; Zhou et al., 2019). Nonetheless, precise polishing technique and

etching procedure are required for precise control of plasmonic resonance. Also, the degraded mechanical strength is undesirable.

Novel optical waveguide structures have been extensively investigated including metal clad waveguide, grating coupling and waveguide coupling with improved sensitivity. An asymmetrical Mach-Zehnder interferometer based RI sensor was proposed with a high sensitivity of  $0.188 \mu\text{m}/\text{RIU}$  in the range from 1.341 to 1.373 (Xia et al., 2017). Recently, a Michelson interferometer was setup to monitor RI of fluidic samples in micro-capillaries operating in the NIR wavelength. This setup has the advantage of dynamic range and the interferometric method is less affected by noise fluctuations (Bello et al., 2020). The simplicity and low cost in the fabrication process of interferometer waveguide have great potential in mass producing RI sensors with higher quality, consistency and efficiency (Tien et al., 2018; Zhang et al., 2020).

Overall, high performance, non-invasive, real time RI sensors that are simple in structure and easy in fabrication are still on demand to develop a faster, simpler and more sensitive that operate in a wide range of telecommunication wavelength.

### **2.3 Multimode Interference Waveguide**

Interferometer sensors utilise the phenomenon of optical interference to measure changes of optical properties that are translated into output intensity or wavelength variations. Interferometer sensors have unique advantages in terms of sensitivity, remote and real-time sensing capability, multi-wavelength analysis, resilience in harsh environments and

immunity to EM interference. The self-imaging effects in interferometers have been exploited in various optical applications including coupler, switch, multiplexer and sensor for their compact structure, low loss, easy fabrication and large fabrication tolerance features (Bahrami, 2017; Ogusu, 2012; Tajaldini & Jafri, 2013).

The structure of MMI is typically composed of a high RI dielectric waveguide sandwiched in between lower RI media. A basic rectangular waveguide as shown in Figure 2.1 consists of three layers constructed with length of MMI,  $L_{MMI}$  and width of MMI,  $W_{MMI}$ . The middle layer, known as the core layer, functions to confine the EM waves propagating from the input to the output waveguide. The upper and lower layers surrounding the core layer, referred as clad and substrate respectively, are responsible to minimise coupling losses by isolating the core layer from the surrounding medium and the wafer it would be assembled on. In this thesis, the index of refraction of the cladding, core, substrate which are  $n_1$ ,  $n_2$  and  $n_3$  respectively are denoted in the order of layer sequence. The index of refraction of the surrounding medium layers is  $n_4$ . The thickness of the core layer is denoted as  $h$  while  $d_1$  and  $d_3$  are the thickness cladding and substrate. The thickness of the layers may vary depending on the footprint desired.

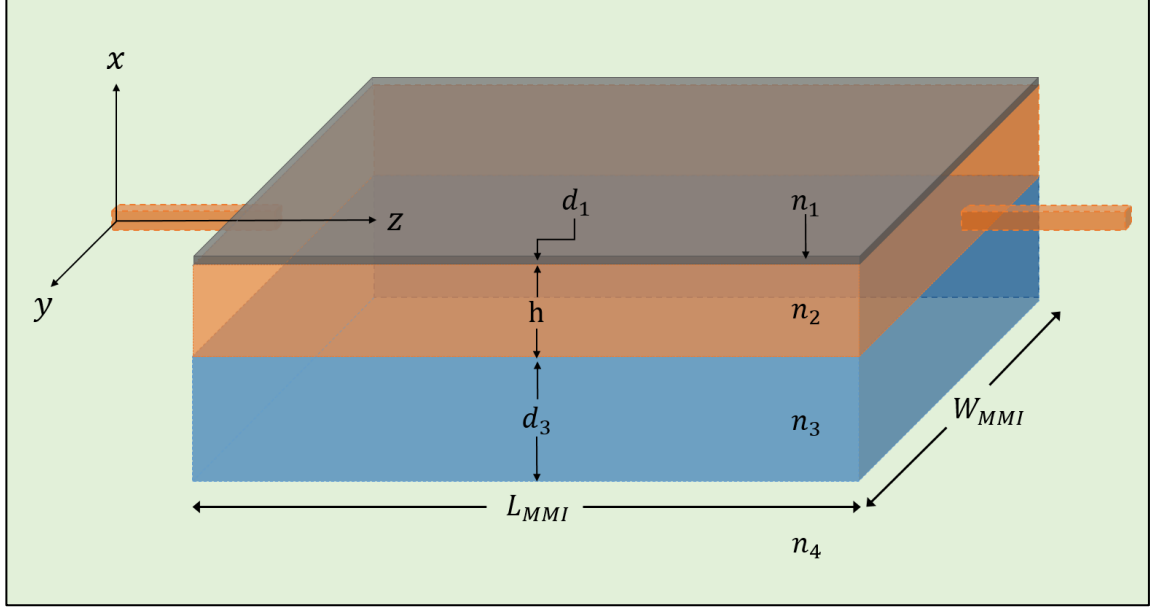


Figure 2.1 Schematic diagram of a dielectric slab waveguide.

The MMI effect is observed from independent propagating modes when an input field,  $\Psi(x, y, z = 0)$  is guided into multimode waveguide in the  $z$ -direction. The  $m$  guided modes propagating at a free-space wavelength,  $\lambda_0$  through the multimode region with propagation constant of the  $m$ -th mode,  $\beta_m$ , interfere with one another to generate a characteristic interference pattern. The interpretation of the self-imaging effect in a multimode waveguide is expressed in Equation (1.1). The input field,  $\Psi$  is expanded in terms of  $m$  guided modes. The field excitation coefficients,  $c_m$  for the  $m$ -th mode can be estimated using overlap integrals. The beat length of the two lowest modes,  $L_\pi$  as expressed in Equation (1.2) is dependent on the effective refractive index,  $N_{eff}$ , effective width,  $W_e$  of the MMI waveguide and wavelength,  $\lambda$  (Soldano & Pennings, 1995).

$$\Psi(x, y, z = 0) = \sum_m c_m \Psi_m(x, y) e^{-j \frac{m(m+2)\pi}{3L_\pi} z} \quad (1.1)$$

$$L_{\pi} \approx \frac{4N_{eff}W_e^2}{3\lambda} \quad (1.2)$$

### 2.3.1 Enhancement Layers for Near Field Sensing

Many studies have employed enhancement layers such as metal, dielectric or semiconductor on optical waveguides to achieve higher sensing performance in the near field. Planar metal-clad waveguides have been shown to achieve high sensitivity by increasing the evanescent field for various bio-sensing applications using reverse symmetry technique (Skivesen et al., 2005). Fouad et al. (2017) found that the high dielectric constant of Barium Titanate ( $\text{BaTiO}_3$ ) deposited on Au enhances the sensitivity of the SPR sensor. Nevertheless, there are still restrictions in micron-scale particles detection and the high loss exhibited by the negative permittivity of metals. Nonlinear materials emerged as compatible media to be integrated in sensing devices in the last two decades. Taya et al. (2009) found that nonlinear media enhance the sensitivity of slab waveguide sensors and thereby proposed slab waveguide structures comprising of left-handed materials.

### 2.3.2 Nanomaterial Integrated Structures

It is desirable to employ enhancement layers with large surface to volume ratio to engineer and tailor high performance sensors. Figure 2.2 shows a) zero-dimensional (0D) nanoparticles consisting of quantum dots and fullerene b) one-dimensional (1D) nanotubes, c) 2D nanosheets including graphene and d) 3D nanostructures including graphite and graphene oxide. The surface properties of low dimensional nanomaterials have gained enormous attention over 3D materials for their excellent sensitivity with

dynamic range. The most popular structure integrated as optical sensors is the 2D nanomaterials. The planar nature of 2D materials has better mechanical flexibility for surface deposition on waveguides compared to the complementary 0D and 1D materials.

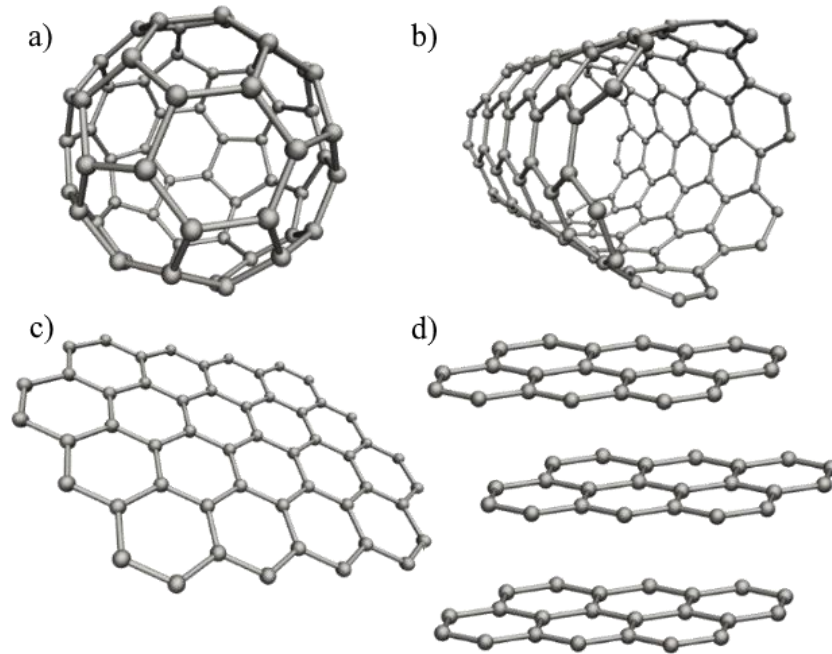


Figure 2.2 Structures of a) zero-dimensional (0D) nanoparticles, b) one-dimensional (1D) nanotubes, c) 2D nanosheets and d) 3D nanostructures.

The common 2D nonlinear materials utilised for optical sensing include graphene (Rastgordani & Kashani, 2020; Sun et al., 2019), transition metal dichalcogenides ( $\text{MoSe}_2$ ,  $\text{MoS}_2$ ,  $\text{WS}_2$  and  $\text{WSe}_2$ ) (Nayeri et al., 2017), metal oxides (Ramgir et al., 2013) and black phosphorus (Abbas et al., 2015) have attracted significant attention over the recent years. Table 2.1 briefly summarised the band structure, optical properties, electrical properties and mechanical stability of various 2D materials reported as RI sensors. Graphene has excellent electrical properties and electron mobility at room temperature due to its zero

bandgap (Bolotin et al., 2008). It stood out as a chemically stable and mechanically robust 2D structure (Barone et al., 2006). The strong nonlinearity of graphene is associated with the exceptionally high third order susceptibility (Cheng et al., 2014). Transition metal dichalcogenides have relatively wide bandgaps ranging from 1 to 2.5 eV and exhibit multiple absorption peaks from ultraviolet (UV) to NIR (Thambiratnam et al., 2020). However, having electron mobility much lower than graphene and being prone to degradation in water as well as UV are some of the drawbacks (Ly et al., 2014). Although monolayer metal oxides exhibit excellent reliability in harsh operating conditions with generally large electron mobility of  $1000 \text{ cm}^2\text{V}^{-1}\text{s}^{-1}$ , their absorption in the visible to NIR region is relatively weak as a result of large bandgaps (Guo et al., 2019). Monolayer black phosphorus has excellent electro-optic properties and high transporter versatility. It has high electron mobility of  $10000 \text{ cm}^2\text{V}^{-1}\text{s}^{-1}$  and direct bandgap of 1.5 eV with the absorption region from UV to infrared (Huang & Ling, 2017; Li et al., 2017). However, it is highly unstable in air which limits its practicality as sensors (G. Wang et al., 2016).

Despite the thin structures, 2D materials have relatively large nonlinear coefficients that contributes to their high sensitivities toward sensing elements such as ions, molecules and metal nanoparticles. A numerical study based on interference of modes in planar multimode optical sensor with an active nanolayer with the RI corresponding to tungsten trioxide ( $\text{WO}_3$ ) material is found suitable as multiple gas sensors (Błahut, 2020). There is a growing scientific interest in using graphene based novel sensing devices and the research community is actively developing sensors to exploit its uniqueness in its electronic and optical properties (Sun et al., 2019).

Table 2.1 Basic properties of most researched 2D materials for optical devices.

Properties	Graphene	Transition metal dichalcogenides	Metal oxides	Black phosphorus
Band gap	Zero bandgap	1 to 2.5 eV	Larger than 2 eV	1.5 eV direct bandgap
Spectral range of optical absorption	Visible to mid-infrared	Multiple absorption peaks from UV to NIR	UV to visible	UV to infrared
Electron mobility ( $\text{cm}^2\text{V}^{-1}\text{s}^{-1}$ )	200000	0.2 to 200	1000	10000
Stability	Chemically stable and mechanically robust	Easily degraded by the presence of oxygen in water and by UV	Excellent reliability in harsh operating conditions	Highly unstable in air

#### 2.4 Optical Properties of Graphene

The unique and versatile properties of graphene have been heavily exploited for photonic and optoelectronic applications including high-speed field-effect transistors, efficient terahertz (THz) sources, ultrafast broadband photodetectors, modulators and plasmonic devices (Bonaccorso et al., 2010; Koppens et al., 2014). Graphene's excellent conductivity and low optical loss have attracted numerous active optical devices including polarisers, optical modulators, sensors and active plasmonic devices that have unfolded promising opportunities in communication, biomedicine and imaging applications (Dai et al., 2019; Luo et al., 2018; Qu et al., 2017; Shushama et al., 2017; Stadler et al., 2011; Sun et al., 2019). The response of graphene to incident EM light is determined by its optical properties. When a monochromatic light with angular frequency,  $\omega$  is incident on

graphene, the intensity and the phase of the incident EM field could be altered due to the separation of charges that results in induced dipole moments. At high optical fields, the atomic and inter atomic field are perturbed. Thus, the response of graphene towards the induced polarisation becomes nonlinear and optical parameters can be modulated.

#### **2.4.1 Linear Optical Properties of Graphene**

Quantitative models have shown that graphene achieve the universal 2.3% linear optical absorption per atomic layer in the visible to NIR spectral range (Bruna & Borini, 2009; Nair et al., 2008). The absorption of a monolayer graphene at normal incidence is equated to the value of the universal dynamic conductivity,  $\sigma_0$  which is equivalent to  $\frac{e^2}{4\hbar}$  over the broad range of photon energies. The absorption is commonly assumed to be directly proportional to the number of layers of graphene. As graphene layers increases, the optical properties of graphene are expected to revert to that of graphite. Nevertheless, Skulason et al. (2010) have experimentally demonstrated that the optical properties of about 700 layers of graphene does not behave as graphite. In the visible to infrared (IR) range, Sasaki and Hitachi (2020) calculated that the number of graphene layers above 1500 layers may be regarded as graphite. The reported values of RI,  $n_{gr}$  and conductivity per layer,  $\sigma_{gr}/\sigma_0$  for monolayer, bulk graphene and graphite that are obtained from various experimental and theoretical methods are tabulated in Table 2.2 for comparison. Since the conductivity of multilayer graphene is expected to change with thickness, conductivity per layer,  $\sigma_{gr}/\sigma_0$  is the optical conductivity of multilayer graphene considered as a stack of independent graphene planes expressed in terms of the fundamental constant  $\sigma_0$ .

Table 2.2 The reported values of refractive index,  $n_{gr}$  and the calculated  $\sigma_{gr}$  for monolayer, multilayer graphene and graphite in literature.

Sample material	Refractive index, $n_{gr}$	Conductivity per layer, $\sigma_{gr}/\sigma_0$	Method	Reference
<b>Monolayer graphene</b>	2.00-1.10i	0.748+0.304i	Reflectance and contrast spectroscopy	(Ni, 2007)
<b>Monolayer graphene</b>	2.37-1.07i	0.862+0.590i	Picometrology	(Wang, 2008)
<b>Graphene and graphite</b>	3.00-1.00i	1.020+1.190i	Reflectance and transmittance	(Bruna, 2009)
<b>Multilayer graphene</b>	2.92-0.77i	0.764+1.179i	Reflectance and transmittance	(Skulason, 2010)
<b>Graphite</b>	2.52-1.94i	1.662+0.270i	Spectroscopic ellipsometry	(Jellison, 2007)
<b>Graphite</b>	3.00-1.38i	1.408+1.036i	Full band theory	(Ahuja, 1997)
<b>Graphite</b>	2.67-1.34i	1.216+0.737i	Picometrology	(Wang, 2008)

Before the discovery of graphene, the optical properties of graphite were investigated theoretically by Ahuja (1997) using the full band theory. Early literatures experimentally measured RI of monolayer graphene via the reflectance method with reflectance spectroscopy setup typically operating in visible wavelengths from 0.40  $\mu\text{m}$  to 0.70  $\mu\text{m}$  (Bruna & Borini, 2009; Ni et al., 2007; Skulason et al., 2010). These reported experimental values made the assumptions of universal optical conductance and constant RI in the visible region. Spectroscopic ellipsometry method is a common technique to investigate optical properties of graphene by measuring changes in polarisation of reflected light at an oblique angle (Jellison et al., 2007; Kravets et al., 2010). A non-

spectroscopic method that does not require elaborate modelling of dispersion is the Picometrology method (Wang et al., 2008) by performing amplitude and phase change measurements. Most literatures (Ghamsari et al., 2016; Yao et al., 2013) validated their experimental measurements by adopting the effective medium theory devised by Vakil and Engheta (2011) that modelled the thickness of graphene. The relative complex permittivity of graphene,  $\varepsilon_{gr}$  as a function of frequency is given in Equation (2.1) (Falkovsky, 2008). The real part of the permittivity measures the ability to store energy, while the imaginary part measures the dissipation of energy (Olhoeft, 1998). The corresponding complex linear optical conductivity of graphene,  $\sigma_{gr}$  can be derived from the Kubo formula given in Equation (2.2).

$$\varepsilon_{gr}(\omega) = \varepsilon_r + i \frac{\sigma_{gr}}{\varepsilon_0 \omega d_{gr}} \quad (2.1)$$

Where  $d_{gr}$  is the thickness of the graphene layer and  $\varepsilon_r$  is the relative dielectric permittivity.

$$\begin{aligned} \sigma_{gr}(\omega) = & \frac{ie^2(2k_B T)}{\pi \hbar^2(\omega + iv_1)} \left\{ \frac{E_f}{2k_B T} + \ln \left( 2e^{-\frac{|E_f|}{k_B T}} + 1 \right) \right\} \\ & + \frac{ie^2}{4\hbar} \left\{ 0.5 + \tan^{-1} \left[ \frac{\hbar(\omega + iv_2) - 2|E_f|}{2k_B T} \right] \right. \\ & \left. - \frac{i}{2\pi} \ln \left[ \frac{[\hbar(\omega + iv_2) + 2|E_f|]^2}{[\hbar(\omega + iv_2) - 2|E_f|]^2 + (2k_B T)^2} \right] \right\} \end{aligned} \quad (2.2)$$

Where  $v_1$  and  $v_2$  are the relaxation frequencies,  $E_f$  is the Fermi level,  $\kappa_B$  is the Boltzmann constant and  $T$  is the temperature. The optical conductivity is reduced to  $\sigma_0$  at low temperatures and zero Fermi level.

It remains a challenge to experimentally obtain the absolute value of  $\sigma_{gr}$  because of the anisotropic nature of graphene. Therefore, the theoretical calculation of  $\sigma_{gr}$  is based on the assumption of universal optical conductance in a wide optical spectrum (Nair et al., 2008). It has been experimentally demonstrated that for graphene layers lower than 150 layers,  $\sigma_{gr}$  is weakly dependent on frequency (Skulason et al., 2010). Considering the thickness of graphene is much smaller than the optical wavelength, the real part of  $n_{gr}$  and the imaginary part of  $\sigma_{gr}$  obtained are rather independent of the number of graphene layers due to the weak interlayer interactions. The real part of  $n_{gr}$  obtained from literatures has a range of values from 2.00 to 3.00 while that of the imaginary part is from -0.77 to -1.94. It is conventional to assign negative sign to the imaginary part describing the attenuation of EM waves through graphene (Smolyaninov, 2018). The negative imaginary part of  $n_{gr}$  is proportional to the number of graphene layers as a consequence of larger absorption with increasing thickness. The real part of  $\sigma_{gr}$  obtained has a range of values from  $0.748\sigma_0$  to  $1.662\sigma_0$  while that of the imaginary part is from 0.270 to 1.190. The quality of graphene samples, substrates and incident wavelengths used may cause discrepancies in the experimental values.

#### **2.4.2 Nonlinear Optical Properties of Graphene**

Graphene's linear dispersion properties of the Dirac electrons enables ultrawideband tunability that lead to strongly nonlinear optical behaviour at microwave and THz frequencies (Mikhailov, 2007). Graphene shows remarkable optical nonlinearities with ultrafast response times and a broadband spectral range. Various nonlinear optical effects of graphene associated with saturable absorption (SA) (Bao et al., 2009), third-harmonic

generation (THG) (Kumar et al., 2013; Yang et al., 2017), four-wave mixing (FWM) (An et al., 2020; Gu et al., 2012), self-phase modulation (Liu et al., 2015) and nonlinear Kerr effect (Vermeulen et al., 2016) have been theoretically and experimentally investigated. Nonlinear frequency conversion to access the visible-NIR wavelength region are of great interest especially in all-optical signal processors and biosensors. Since the second-order nonlinear optics effects are not allowed in graphene due its centrosymmetric crystal, THG is one of the most fundamental manifestations of graphene's nonlinear optical response. THG was experimentally observed in graphene and graphite flakes with large third-order susceptibility,  $\chi^{(3)}$  (Hendry et al., 2010; Kumar et al., 2013). This large  $\chi^{(3)}$  originated from the interband electron transitions is approximately eight orders of magnitude larger than the dielectric materials (Demetriou et al., 2016).  $\chi^{(3)}$  is an intrinsic property of a nonlinear medium that describes the generated third-order nonlinear optical interactions. Most literature treats graphene as a thin film since it is more convenient to work with bulk rather than its surface properties especially in computational methods (Hendry et al., 2010; Kumar et al., 2013; R. Wu et al., 2011). Thus, the interaction of external applied EM field with a nonlinear medium is described by effective susceptibility,  $\chi_{eff}$  as expressed in terms of the linear susceptibility,  $\chi^{(1)}$  and the nonlinear susceptibility in Equation (2.3).  $\chi_{eff}$  is proportional to the square of the strength of the applied static electric field,  $E(\omega)$ . The linear susceptibility  $\chi^{(1)}$  is related to the linear RI,  $n_0$  is as given in Equation (2.4) (Boyd & Prato, 2008).

$$\chi_{eff} = \chi^{(1)} + 3\chi^{(3)}|E(\omega)|^2 \quad (2.3)$$

$$n_0 = (1 + \chi^{(1)})^{1/2} \quad (2.4)$$